# Machine Learning-Assisted probabilistic fatigue evaluation of Rib-to-Deck joints in orthotropic steel decks

Heng, Junlin; Zheng, Kaifeng ; Feng, Xiaoyang; Veljkovic, Milan; Zhou, Zhixiang

**DOI**
10.1016/j.engstruct.2022.114496

**Publication date**
2022

**Document Version**
Final published version

**Published in**
Engineering Structures

Engineering Structures 265 (2022) 114496

Contents lists available at ScienceDirect

Engineering Structures

journal homepage: www.elsevier.com/locate/engstruct

# Machine Learning-Assisted probabilistic fatigue evaluation of Rib-to-Deck joints in orthotropic steel decks

Junlin Heng [a,b], Kaifeng Zheng [c], Xiaoyang Feng [c], Milan Veljkovic [b], Zhixiang Zhou [a,*]

[a] Department of Civil Engineering, College of Civil and Transportation Engineering, Shenzhen University, Shenzhen 518060, China
[b] Department of Engineering Structures, Faculty of Civil and Environment Engineering, Delft University of Technology, Delft 2628 CN, the Netherlands
[c] Department of Bridge Engineering, School of Civil Engineering, Southwest Jiaotong University, Chengdu 610031, China

ARTICLE INFO

*Keywords:*
Orthotropic steel decks
Rib-to-deck joints
Probabilistic fatigue assessment
Gaussian process regression
dynamic Bayesian network

ABSTRACT

This study integrates the fatigue test and numerical prediction to derive a comprehensive probability-stress-life (P-S-N) curve for rib-to-deck (RD) welded joints in orthotropic steel decks. Fatigue tests of RD joints are conducted to measure fatigue strength and crack growth data. Based on the test, a probabilistic fatigue crack growth (PFCG) model is established to predict the distribution of fatigue life under various stress ranges. Two machine learning tools are adopted to assist the PFCG model-based prediction, i.e., the Gaussian process regression (GPR) and dynamic Bayesian network (DBN). The GPR is used to train a surrogate model solving stress intensity factors for the PFCG prediction, using 2,000 samples generated from finite element (FE) analyses. The trained model is then validated by a new dataset of 100 FE samples. An adapted DBN model is proposed to update the PFCG model with the fatigue crack growth data measured from ten specimens. According to the result, the application of GPR can reduce the solution cost of the PFCG prediction by approximately 1,875 times. Compared with the prior PFCG model, the updated posterior model shows an improved agreement with the test data, i.e., the maximum difference in fatigue strength between model prediction and test data decreases from 12% to 3%. Based on the posterior PFCG model, the P-S-N curve of RD joints is statistically derived using sufficient numerical samples.

## 1. Introduction

### 1.1. Research background

Long-term deterioration analysis is the core supporting the life-cycle management of bridges to meet the designed serviceability [1]. Especially, orthotropic steel decks (OSDs) in steel bridges are of particular concern due to premature fatigue cracking after several decades of exploitation under vehicle loads [2]. OSDs are highly integrated structural systems fabricated with numerous welded joints [3]. Among the joints, the rib-to-deck (RD) joint has the longest welding length (e.g., 50 times the bridge length) and is prone to fatigue, highlighting the importance of its fatigue deterioration prediction [45].

### 1.2. State-of-the-art

#### 1.2.1. Probability-stress-life curves for fatigue deterioration analysis

Due to the significant complexity and uncertainties in fatigue of bridge joints, existing prediction approaches are mainly based on probability-stress-life (P-S-N) curves derived statically from fatigue tests [6]. For example, Pipinato et al. [7] performed fatigue tests of riveted joints removed from an aged steel bridge to investigate its fatigue cracking pattern and P-S-N category. On this basis, remain fatigue life of the joint was estimated [8]. However, it is budget- and time-consuming to construct the P-S-N curves by fatigue tests. The P-S-N curve usually employs the nominal stress that only covers the global behaviour of a specific joint type [9]. As a result, sufficient specimens are required for each type [10]. The advanced hot-spot stress approach can ease the situation by partially including the local behaviour to improve the transferability between similar joint types [11]. However, the number of specimens still plays a crucial role, and it is left to a designer's own experience to judge the transferability.

#### 1.2.2. Fracture mechanics to predict fatigue crack growth - deterministic approaches

Fracture mechanics (FM) has been applied as a promising alternative

* Corresponding author.
*E-mail address:* zhixiangzhou@szu.edu.cn (Z. Zhou).

https://doi.org/10.1016/j.engstruct.2022.114496
Received 30 July 2021; Received in revised form 10 April 2022; Accepted 30 May 2022
Available online 9 June 2022

to fatigue tests of welded joints [12]. The FM explicitly simulates fatigue crack growth in joints and shows less dependence on test data. Xin and Veljkovic [13] suggested the feasibility of FM in predicting fatigue crack growth in welded joints based on test data of smooth coupons. Malschaert [14] validated the application of finite element (FE)-based FM simulation in fatigue prediction of welded joints in steel bridges. Liu et al. [15] hired the FE-based stress analysis and FM simulation to investigate fatigue crack growth in RD joints. According to the result, the crack remains semi-elliptical, whereas the aspect ratio of crack depth to length decreases with the increase in crack sizes. Wang et al. [16] combined the analytic solution-based FM model with traffic monitoring data to investigate the fatigue performance of RD joints. Different control strategies were investigated, and damage-based permit checking was proposed for a trade-off between durability and serviceability of the bridge.

Generally, the FE-based fracture analysis requires extensive efforts in re-modelling and re-meshing the crack body during growth [12 17]. This can be overcome by applying the extended finite element method (XFEM), which enables automatic fatigue crack growth without re-meshing [18]. Nagy et al. [19] employed the XFEM to simulate fatigue crack growth in RD joints, validating its application in fatigue evolution. Similarly, Gupta et al. [20] combined the XFEM and virtual crack closure technique (VCCT) to predict the fatigue life of welded connections in an aged bridge, wherein a satisfying agreement was observed between the prediction and inspection. As a matter of fact, the XFEM needs a highly refined meshing for the assumed cracking region to keep the simulation stable and converge, which escalates the computational complexity and even makes it intractable in probabilistic simulations.

#### 1.2.3. Fracture mechanics analysis with probabilistic modelling

All the above works uses the deterministic FM analysis, which contradicts the random nature of fatigue cracking [21]. As a solution, the FM could be hired with probabilistic modelling. Righiniotis and Chrysanthopoulos [22] established the probability distribution of fracture parameters and conducted the probabilistic assessment using the analytical FM solution to derive the P-S-N curve of four typical joints. The result showed a good agreement with codes-of-practice. Liu and Mahadevan [23] proposed a probabilistic method of fatigue prediction using the analytical FM solution and equivalent initial flaw size (EIFS). The distribution of EIFS was established based on the fatigue test data. Heng et al. [24] presented an FM-based probabilistic assessment approach of the RD joint using the analytical solution of SIFs. Through the approach, a large dataset of P-S-N was generated to derive the P-S-N curve of RD joints.

A common feature of the above works is that the analytical solution was applied instead of FE simulations. This can be explained by the exhaustive solution efforts in the probabilistic fatigue crack growth (PFCG) simulation. Due to significant uncertainties in fatigue, the PFCG simulation requires a large sample size, e.g., $10^6$ or even more. As a result, the FE simulation becomes numerically intractable. However, the analytical solutions are derived for specific joints with specific configurations [25], of which the adaptability is open to discussion.

#### 1.2.4. Integration of model prediction and test result

Because of the aleatory uncertainty in fatigue deterioration and epistemic uncertainty in modelling, intrinsic gaps exist between the fatigue model prediction and test data [26]. The gap could be filled by integrating the numerical model and physical data. Straub [27] proposed a general framework of Dynamic Bayesian networks (DBNs) for the condition-based deterioration analysis. Zhu et al. [28] proposed a DBN framework for the fatigue diagnosis and prognosis of OSD and proved its feasibility via a case study. Heng et al. [29] established a primary DBN model for condition-based fatigue prediction of welded joints in steel bridges, which includes inspection results. Hu et al. [30] employed the Markov Chain Monte Carlo to update parameter distributions of the fatigue prediction model based on new test data. Silva et al. [31] used the extremely randomised tree to train a fatigue prediction model by integrating FE predictions and a collected test dataset. The trained model showed improved accuracy and generalisation ability in fatigue life prediction. Several up-to-date methods are also available to integrate the model and data, e.g., physic-guided neural network [32] and Bayesian deep learning [33]. However, the feasibility of these methods in fatigue prediction is still open to discussion.

### 1.3. Existing research gaps

Apart from the above efforts, notable research gaps still exist as follows.

(1) A comprehensive P-S-N curve of RD joints is required for its long-term fatigue evaluation. The curve can be derived by fatigue tests of enough specimens, but it is budget- and time-inefficient.

(2) The fracture mechanics could be combined with probabilistic modelling to establish the P-S-N model numerically. However, the need for a large sample size restricts the application of FE simulations. Analytical solutions can be applied to reduce the solution complexity, but it raises concerns about the adaptability and transferability of various solutions.

(3) Machine learning algorithms can integrate the fatigue model prediction with physical test data to bridge their intrinsic gap. Nonetheless, previous efforts are at the framework- or prototype-level, lacking the application in solving practical assignments.

### 1.4. Aim and methodology of the study

This study aims to derive a comprehensive P-S-N curve of RD joints in OSDs, which supports the long-term fatigue evaluation. Fatigue tests and FE-based fracture analyses have been conducted and integrated via two machine learning tools, i.e., the gaussian process regression (GPR) and dynamic Bayesian network (DBN). 2,000 FE samples are used for the GPR-based model training, whereas the DBN-based updating utilises the fatigue crack growth data from ten specimens. The output not only provides a reference for the related research, design, and fabrication of welded connections but also highlights the application of machine learning in solving the traditional structural issue.

## 2. Fatigue tests of rib-to-deck specimens

### 2.1. Design of specimens

Fatigue model tests have been carried out to investigate the fatigue cracking feature of RD joints, as shown in Fig. 1. Seven specimens are fabricated, including two specimens with conventional U-rib (called type-C) and five specimens with thickened edge rib (called type-T). The type-T has an improved welding penetration depth in the RD joint, which enhances its fatigue performance [32]. The specimen has a length and width of 1000 mm and 600 mm, respectively. The 16 mm-thick deck plate and 8 mm-thick trapezoidal rib (of which the edge is thickened to 12 mm in type-T specimens) are connected via two RD joints. The structural steel Q345qD [34] (similar to S355NL [35]) is used in accordance with the matched welding wire ER50-6 [36]. Table 1 lists the basic mechanical properties of used materials.

Submerged-arc welding by a semi-auto welder is used to fabricate all specimens together in an assembly. The assembly is then cut into seven specimens via electrical discharge machining. During welding, the RD joint undergoes an uneven heating-and-cooling process with restraints. The associated thermal-to-mechanics process results in significant welding residual stress in the RD joint [37]. Thus, the same welding parameters are used for all the specimens to keep the residual stress consistent. The welding current, voltage, and travel speed are 290 $\pm$ 20 A, 29 $\pm$ 2 V, and 380 $\pm$ 20 mm/min, respectively.

The three-point bending boundary has been employed to minimise the thermal stress induced by variation in ambient temperature. The

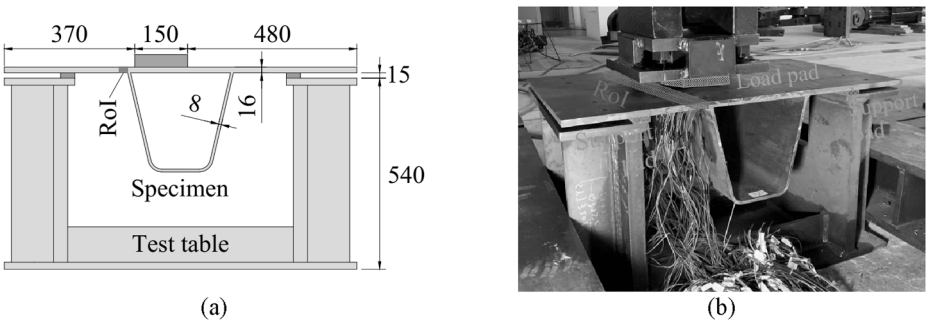


**Fig. 1.** Test specimen and setup: (a) Schematic; (b) Photography.

**Table 1**
Basic mechanical properties of materials.

| Material | Grade | Elastic modules (MPa) | Yield strength | Ultimate strength | Elongation after fracture |
|---|---|---|---|---|---|
| Base | Q345qD | $2.06 \times 10^5$ | 345 | 490 | 0.20 |
| Weld | ER50-6 | $2.06 \times 10^5$ | 432 | 573 | 0.31 |

specimen is supported on a rigid test table, with two rubbery pads inserted between the specimen and table, as shown in Fig. 1. In order to simulate the critical state of RD joints, the actuator is placed close to the left joint, marked as the region of interest (RoI) in red in Fig. 1. Similarly, a rubbery pad is installed between the deck and actuator to distribute applied loads.

### 2.2. Test implement

An MTS servo-hydraulic machine [38] is used to generate the sinusoidal cyclic loads in constant amplitude. Since the loading frequency by servo-hydraulic machines is usually less than 100 Hz, the frequency shows a minor effect on the fatigue behaviour of steels without strong corrosion [39 40]. Thus, the loading frequency is set as 4 Hz to facilitate the test implementation and measurement. Moreover, the test has been conducted in a structural laboratory during the daytime, by which the effect of thermal stress and corrosion could be minimised. Due to the prominent welding residual stress in RD joints, the stress ratio-dependent fatigue enhancement could be omitted according to IIW [9]. To this end, the ratio of minimum load to maximum load is determined as roughly 0.3 for all the specimens. The applied loads are varied to produce test data under different stress ranges, as shown in Table 2. In the previous studies [4 24 41], a total of 11 specimens with the same configuration were tested, including 5 type C specimens and 6 type T specimens. For the consistent purpose, the specimens in this study are numbered from C6 and T7 for the type-C and type-T, respectively.

According to the survey on a list of similar fatigue tests [24 42 43], the strain near cracking sites drops proportionally with the increase in crack depth. Thus, the strain drop has been monitored along the joint by installing an array of strain gauges near the deck toe, as shown in Fig. 2. Both the nominal and hot-spot stress ranges are considered in deriving

**Table 2**
Loading protocols (Unit: kN).

| ID | $F_{max}$ [1] | $F_{min}$ [2] | $\Delta F$ [3] | ID | $F_{max}$ | $F_{min}$ | $\Delta F$ |
|---|---|---|---|---|---|---|---|
| C6 | 15 | 50 | 35 | T9 | 19 | 65 | 46 |
| C7 | 15 | 50 | 35 | T10 | 19 | 65 | 46 |
| T7 | 15 | 50 | 35 | T11 | 22 | 74 | 52 |
| T8 | 18 | 60 | 42 | | | | |

[1] : Maximum load;
[2] : Minimum load;
[3] : Load range

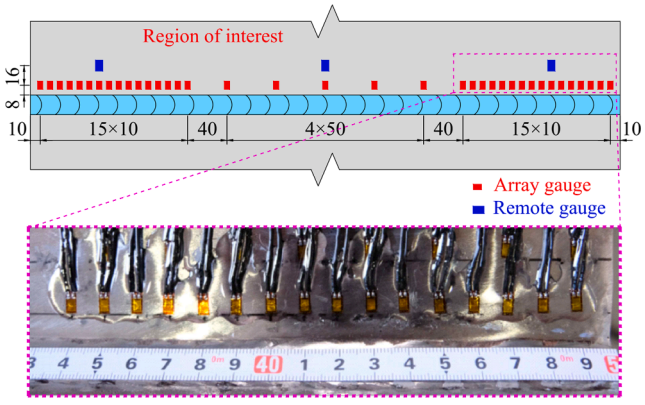


**Fig. 2.** Strain gauges installed at the region of interest.

the fatigue strength of RD joints. The hot-spot stress is determined by the "0515" criteria suggested by IIW [11], as shown in Equation (1):

$$\Delta\sigma_{hs} = 1.5 \bullet \Delta\sigma_{0.5t} - 0.5 \bullet \Delta\sigma_{1.5t} \quad (1)$$

where $\Delta\sigma_{hs}$ denotes the hot-spot stress range; $t$ is thickness of deck, i.e., 16 mm; $\Delta\sigma_{0.5t}$ and $\Delta\sigma_{1.5t}$ are the stress range measured at the points $0.5t$ (8 mm) and $1.5t$ (24 mm) away from the deck toe.

The nominal stress range is determined by remote gauges ($\Delta\sigma_{1.5t}$) due to the ignorable notch effect at that distance [11]. Meanwhile, the strain measured in an un-loaded steel plate is used for temperature compensation. The strain range is recorded for 1 min every half an hour (about 7,200 cycles). According to Luo et al. [44], a limit of 5% drop in strain ranges has been hired to identify cracking during the test. Besides the strain drop, the dye penetration (DP) check [45] is also performed to detect fatigue cracks. At the early stage, the DP check is conducted every 50,000 cycles. After cracking is confirmed, the check is carried out every 10,000 cycles. Once the crack penetrates through the thickness of the deck, the test is terminated, and the corresponding number of loading cycles is regarded as fatigue endurance.

### 2.3. Test result

The weld toe-to-deck cracking has been observed in all seven specimens, as shown in Fig. 3. The crack initiates at the weld toe on the bottom of the deck and then grows with cycles in both the thickness and length directions. In the elevational view, one or two symmetrical cracks have been observed, of which the cracking centre was about 100 ~ 150 mm away from the specimen edge.

The measured stress range and the number of cycles are summarised in Fig. 4a and b, along with the test data of 11 specimens from the previous studies [42441]. Based on the data, the mean S-N curve is derived and included in Fig. 4. Due to the limited number of specimens, the power index of $m = 3$ is applied in the derivation, as suggested by [9]. According to the result, the fatigue strength of RD joints is notably

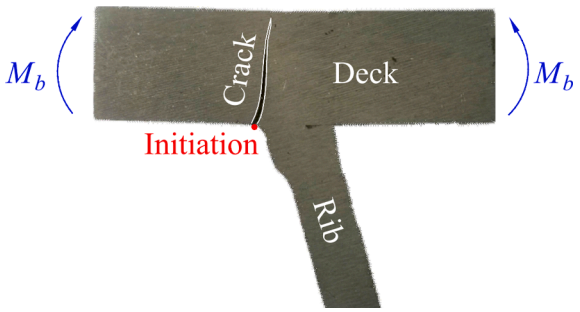


**Fig. 3.** Fatigue cracking pattern of RD joints.

higher in type-T specimens than that in type-C specimens. In the case of nominal stress, the mean fatigue strength at 2 million cycles is 124 MPa in type-T and 102 MPa in type-C, i.e., 22 % improvement in Type-T. A similar result can be found in hot-spot stress, wherein the mean strength increases by 20% in type-T (from 128 MPa to 154 MPa) compared with type-C.

Fig. 5 lists the drop percentage in strain ranges installed along the deck toe. As discussed in Section 2.2, the strain drop can approximate the crack depth. Furthermore, by introducing a strain drop limit of 5% to identify crack initiation, the crack length can be estimated by the interval length between crack-initiated points. Due to the malfunction of several key gauges in specimen C7, its monitored data has been excluded. The result shows that single-cracking is observed in all the specimens but T10, in which two distinct cracks are observed. However, another minor crack (or flaw) may also co-exist in these specimens but may be too small to identify by the strain drop. During the growth, the fatigue crack stays almost semi-elliptical. The crack growth rate is relatively slow at the early loading stage, while it becomes more and more rapid with the number of cycles. The growth rate is remarkably higher in the crack length than in the crack depth. As a result, the aspect ratio of crack depth to length declines with the number of cycles, as shown in Fig. 5.

It is very interesting to note that the measured fatigue crack shape and its variation during the growth are highly comparable with the numerical prediction in [15]. Apart from the listed measurement, additional fatigue crack growth data can also be found in the previous experiment [24], in which four specimens were fabricated with the same configuration and tested under a similar boundary condition. Those data will also be incorporated in the subsequent investigation due to the high similarity.

## 3. Probabilistic fatigue crack growth model

### 3.1. Fatigue crack growth model

Based on the test, the fatigue crack growth (FCG) model has been established using the fracture mechanics, as shown in Fig. 6. Two crack-like initial flaws are assumed at the deck toe, named C1 and C2, with the centre sited 125 mm away from the edge. In accordance with the test observation, semi-elliptical cracks are assumed in the FCG model. Thus, the crack is idealised by a two degree-of-freedom (DOF) model consisting of the crack depth $a$ and crack half-length $c$.

The stress intensity factors (SIFs) at the crack tip and edge is assumed to as the major driven force for the crack growth. The modified Paris rule [46] has been employed to predict the crack growth per cycles, as illustrated in Equation (2):

$$\frac{da}{dN} = C \bullet (\Delta K_a - \Delta K_{th})^m, \frac{dc}{dN} = C \bullet (\Delta K_c - \Delta K_{th})^m \tag{2}$$

where $a$ and $c$ are the crack depth and half-length, respectively; $N$ is the number of loading cycles; $C$ and $m$ are the crack growth rate and power index; $\Delta K_a$ and $\Delta K_c$ are the SIF range at the crack tip and edge, respectively; $\Delta K_{th}$ is the fatigue limit below which the crack arrests.

Based on Equation (1), the fatigue life can be solved by integrating the crack depth and length from initial to critical size. For numerical implementation, the above integration is approximated by a series of discrete solution steps with a small increment in crack sizes (e.g., this study uses a limit of 0.01 mm and 0.1 m in crack depth and length, respectively), as shown in Equation 3:

$$\begin{aligned} a_t &= \sum_{i=0}^{n_t} (C \bullet (\Delta K_a - \Delta K_{th})^m) \bullet \Delta N_i \\ c_t &= \sum_{i=0}^{n_t} (C \bullet (\Delta K_c - \Delta K_{th})^m) \bullet \Delta N_i \end{aligned} \tag{3a-3b}$$

where $a_t$ and $c_t$ are respectively crack depth and half-length at time $t$; $n_t$ is the number of discrete solution steps; and $\Delta N_i$ is the increment in the number of cycles at $i$th solution step, which meets the requirement of the limit in crack size increment.

### 3.2. Probabilistic modelling of fracture parameters

The proposed FCG model is combined with probabilistic modelling to establish a probability fatigue crack growth (PFCG) model for RD joints. In the PFCG model, the uncertainty in the initial flaw size and Paris law is modelled via random variables. The initial flaw size is expressed by the initial flaw depth and the ratio of depth to length, through which the correlation between the flaw depth and length is implicitly simulated [46]. The initial flaw size distribution is decided after [47], as shown in Fig. 7a and b. Since the crack growth rate and power index are correlated, the uncertainty is fully included in the growth rate while the power index is set as 3, as suggested by [46]. Similarly, the crack growth rate is reproduced using the mean and design value from BSI 7910 [46], as shown in Fig. 7c. In the case of fatigue limit, the distribution is determined after [48], as shown in Fig. 7d.

### 3.3. Computational procedures of the PFCG model

The proposed PFCG model is calculated in two steps, as shown in

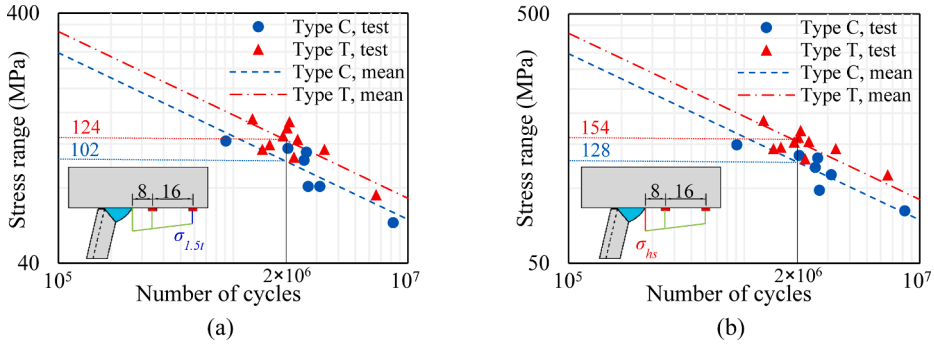


**Fig. 4.** S-N results of the two types of specimens: (a) Nominal stress; (b) Hot-spot stress.

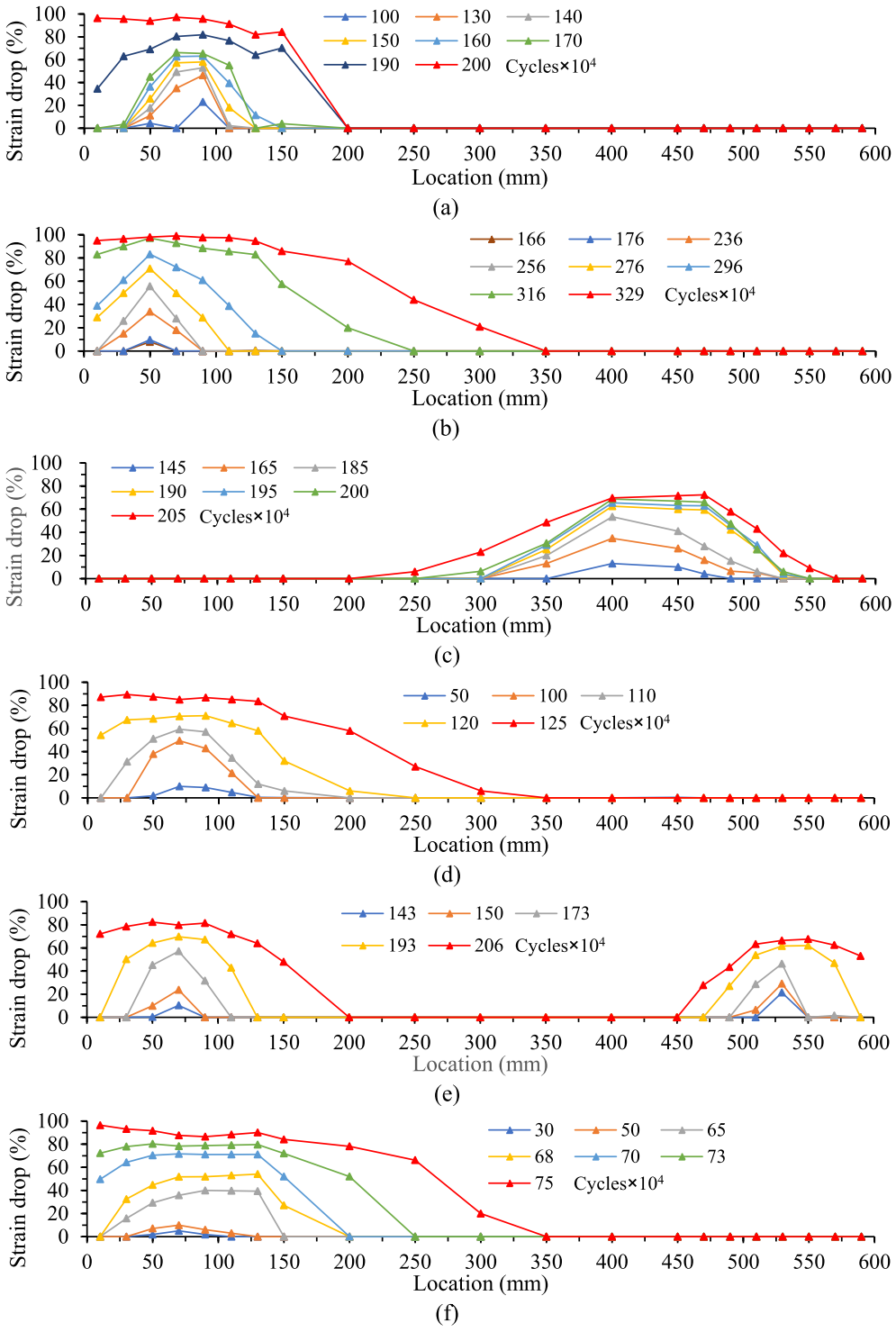


**Fig. 5.** Measured strain drops in different specimens: (a) C6; (b) T7; (c) T8; (d) T9; (e) T10; (f) T11.

Fig. 8. In the first step, the sampling of variables is conducted using the probabilistic distributions in section 3.2. Since two initial flaws, C1 and C2, are assumed, the sampling of flaw sizes is independently carried out for the two flaws. Meanwhile, the two flaws share the sampled crack growth rate and fatigue limit since they are within the same specimen. Based on the sampling, fatigue crack growth is simulated via fracture mechanics.

As the continuous probability distribution has been applied, there is an extremely small probability that the initial flaw exceeds the critical size. This is of no doubt a mathematical issue in numerical simulation, which is abnormal and impossible in reality. In this case, the sample is also regarded as a run-out. Otherwise, the cracking-driven force, SIFs, will be calculated to predict the increment in crack sizes via the modified Paris law in Equation (1). Since fatigue limit is used, the crack arrest occurs when the SIFs are below the limit, and the sample is also treated as the run-out. Else, the simulation continues to the next loop until the critical size is reached.

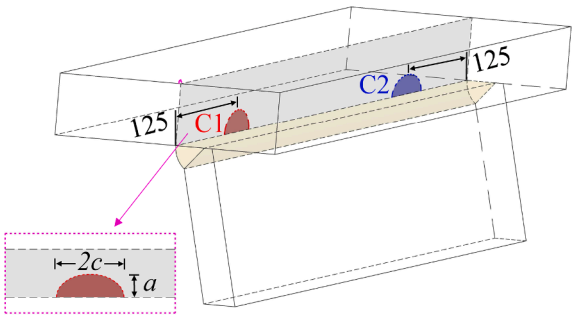


**Fig. 6.** Fatigue crack growth model.

## 4. GPR-assisted fracture analysis

In this part, a Gaussian process regression (GPR) model of SIFs prediction is trained and validated by a dataset generated from FE-based fracture analyses. With the GPR model, the PFCG simulation can be conducted with a satisfactory trade-off between accuracy, efficiency, and flexibility.

### 4.1. Parametric FE-based fracture analysis

FE models of the test specimen have been modelled using the software ANSYS-APDL [49], as shown in Fig. 9. The multi-scale modelling has been used to achieve a trade-off between efficiency and accuracy. The FE model consists of three parts, i.e., the global model, sub-model, and crack body. The global model is used to transfer the boundary and the stress conditions to the crack body. Thus, it is meshed with a relatively coarse element size, i.e., 4 × 4 mm in cross-section and 8 mm in length. Between the relatively coarse global model and highly refined crack body, a refined sub-model is constructed to provide a smooth transition in element sizes. A user-subordinate is coded to mesh the sub-model and crack body automatically with various crack sizes. Especially, the user-subordinate adopts an adaptive meshing strategy that varies the element size from 5% of the crack depth to 2 mm in the out layer of the sub-model. Surface-to-surface contact [50] is used to coordinate the nodal displacement between the global model and sub-model, whereas the crack body is connected to the sub-model via sharing nodes.

The fatigue cracking of RD joints falls into the region of high-cycle fatigue (HCF), since the number of loading cycles is well above $10^4$. Thus, the linear-elastic material model is applied in the FE simulation as suggested by Taylor and Hoey [51]. The properties of the material model are determined according to Table 1. Because of the application of the two DOFs crack model (see Fig. 6) and linear-elastic material model, the SIF at the crack tip ($\Delta K_a$) and edge ($\Delta K_c$) can be expressed by Equation (4):

$$\Delta K_a = \Delta\sigma \bullet Y_a(a,c) \bullet \sqrt{\pi a}, \Delta K_c = \Delta\sigma \bullet Y_c(a,c) \bullet \sqrt{\pi a} \# \tag{4}$$

where $a$ and $c$ are crack depth and half-length, respectively; $\Delta\sigma$ denotes the applied stress range; $Y_a$ and $Y_c$ represent the correction factor at the crack tip and edge, respectively.

Based on the above equation, the crack depth $a$ and half-length $c$ is selected as input features in training the GPR model. The output label is determined as the normalised SIF range $\overline{\Delta K}$ solved under the unit stress of $\Delta\sigma = 1MPa$, which increases the generalisation ability of the model. To this end, the FE analysis aims at the derivation of SIFs for cracks with various depths and lengths. This requires no re-meshing effort due to pre-assignment of fatigue cracks. The contour integral (CI) [52] is leveraged in solving the above SIFs. The CI has an improved solution efficiency over the XFEM, despite the need for a pre-defining cracking path. A total of 6 contours are integrated, and the SIF is determined by averaging the second to sixth contours that show stability and consistency.

The minimum and maximum crack depth are respectively set as 0.1 mm and 15 mm (from 0.6% to 94% deck thickness), due to the limitation in meshing capacity of the FE model. Similarly, the crack length is limited to the minimum value between 50 times crack depth and 120 mm. The number of values is determined as 50 for crack depth and 40 for length. Thus, the parametric FE analysis generates a dataset of 50 × 40 = 2,000 points in total, as listed in Table 3. As shown by Equation (1), the crack grows at an escalating rate with the increase in crack size. To this end, the non-uniform interval is utilised in the discretisation to densify the training data points at the region of small crack size.

### 4.2. Construction and application of GPR surrogate model

The Gaussian process regression (GPR) [53] is a powerful machine learning tool, by which the prediction can be made based on the covariance of inputs. In the GPR, the covariance between data points is expressed in terms of the kernel function [54]. The method assumes that the overall response consists of an explicit basis function and a latent function, as expressed by Equation 5:

$$\begin{aligned} g(\dot{x}) &= \xi(\dot{x})^T\dot{\theta} + f(\dot{x}) \\ f(\dot{x}) &\sim GP(0, r(\dot{x}, \dot{x}^{'})) \end{aligned} \tag{5a-5b}$$

where $g(\dot{x})$ is the basis function on a $n_d \times 1$ input vector $\dot{x}$; $\dot{\theta}$ is a $n_p \times 1$ vector about the factors in the basis function; $\xi(\dot{x})$ stands for the explicit function to transfer $\dot{x}$ from $\mathbb{R}^{n_d}$ to $\mathbb{R}^{n_p}$ space; $f(\dot{x})$ is the lament function following the zero-mean Gaussian process; and $r(\dot{x}, \dot{x}^{'})$ is the kernel function depicting the covariance between input vectors.

Fed with training data, the parameters in both basis and latent functions of the GPR model could be derived via the maximum likelihood estimation. Herein, predictions can be made using the trained GPR model at new inputs. The GPR can be regarded as an updated version of the Kriging interpolation [55] that is widely applied in Geostatistics, except for a slight difference in their mathematic expression. Another alternative to the GPR is the deep neural network (DNN), which is very hot now. The DNN can handle big data but needs iterative optimization of parameters such as weights and biases. Unlike the DNN, the GPR is a nonparametric method that avoids iterations. However, the GPR is limited in dealing with massive data due to its computational complexity of $O(N^3)$ [54]. Due to the limited train data (i.e., 2,000 points) in this study, the GPR is suitable and selected for training the

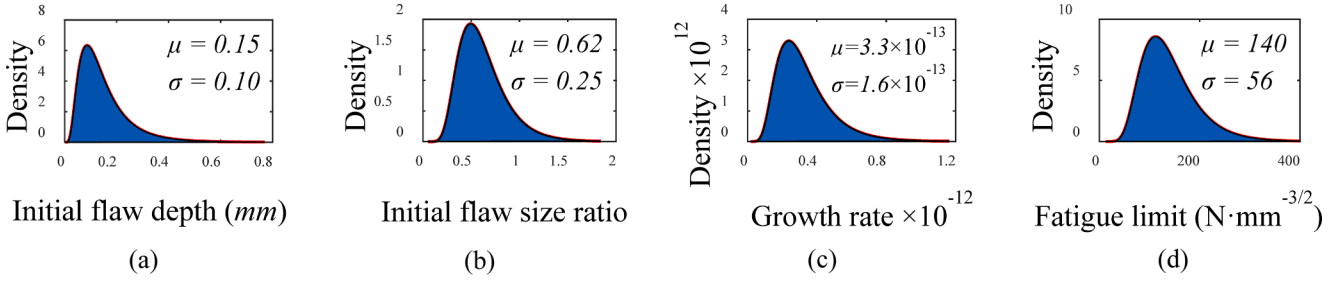


**Fig. 7.** Probability distribution of fracture parameters: (a) Initial flaw depth [47]; (b) Initial flaw size ratio [47]; (c) Crack growth rate [46]; (d) Fatigue limit [48].

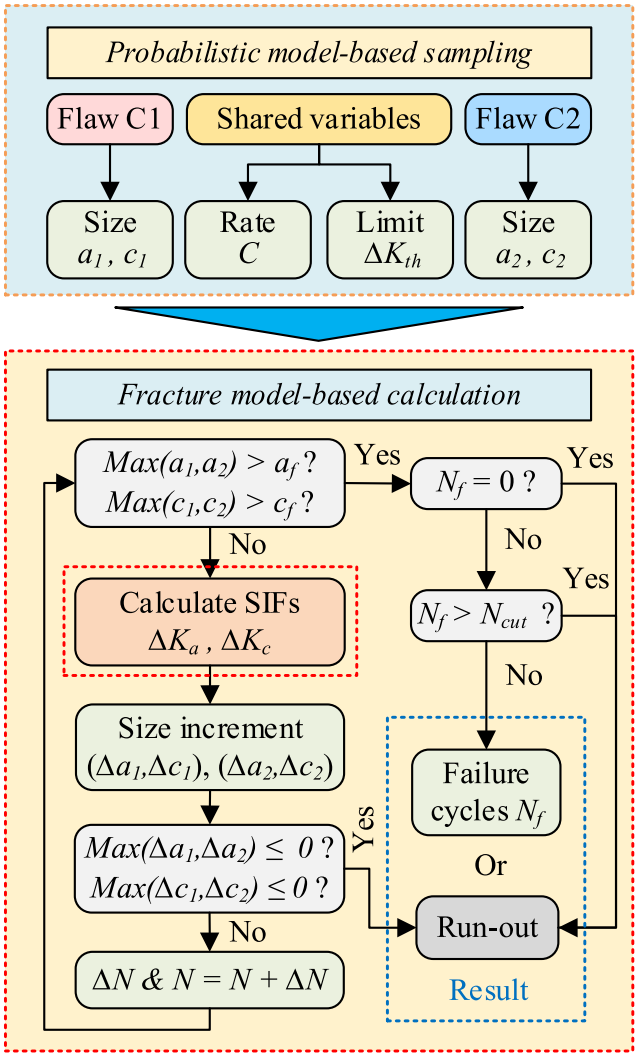


**Fig. 8.** Computational procedures of the PFCG model.

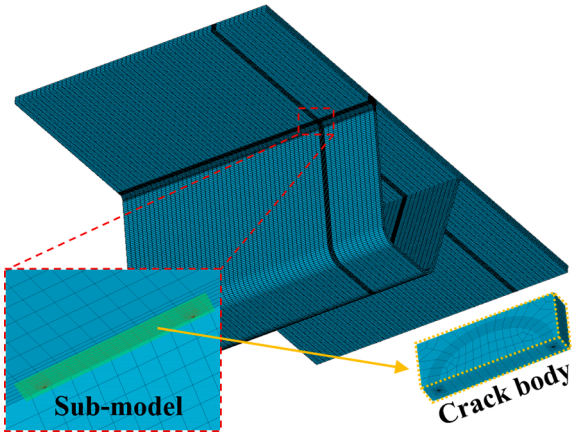


**Fig. 9.** Multi-scale FE model with crack body.

surrogate model.

Although numerous efforts are avoided to optimise model parameters by the GPR, the selection of kernel functions is still required among several available types. In general, the kernel functions could be classified into two types: (1) the function with a uniform length scale; (2) the automatic relevance determination (ARD)-based function with separate

**Table 3**
Range of parametric FE analysis.

| Variable | Symbol | Range (*mm*) | $N_v$ | $D_V(v)$ [2] |
|---|---|---|---|---|
| Crack depth<br>Crack length | $a$<br>$c$ | 0.1 ~ 15<br>a ~ min(50a,120) | 50<br>40 | $exp(a)$<br>$exp(c)$ |

[1]: Number of values
[2] : Discretisation function;

length scales on each predictor. The commonly used kernels include the exponential (Exp), squared exponential (SE), Matern32 (Ma32), Matern52 (Ma52), Rational Quadratic (RQ), and their ARD-based form. Comparisons have been conducted to investigate the influence of the above kernels. A total of 100 testing data points are sampled and calculated using the FE model. The performance of different kernels is evaluated via the root mean square error (RMSE), as shown in Fig. 10. The first letter "C" and "T" respectively denote the type C and T specimens, followed by the words "$K_a$" and "$K_c$" depicting the SIFs at the crack tip and edge.

The result shows that all the minimum RMSE is obtained under the ARD-Exp kernel. Thus, the kernel has been employed in the subsequent study. Meanwhile, the RMSE is no larger than 0.31 between the GPR prediction and test, which validates the effectiveness of the trained GPR model to surrogate the FE-based fracture analysis. For better visualisation, the GPR model of type C specimens is plotted in Fig. 11, along with the training and testing data. After the training and validation, the GPR models can be used to calculate the SIFs required in the PFCG model.

Fig. 12 summarises the overall procedures to construct and apply the GPR model. With the GPR model, solution costs can be effectively reduced, which enables the implementation of the PFCG model. For instance, one FCG simulation may take about 300 ~ 500 solution steps. When using a 10-cores workstation (Intel i9-10900 K), roughly 150 s are required for a single step. In total, around 45,000 ~ 75,000 s (12.5 ~ 20.8 h) will be spent in predicting one datapoint. It is true that the FE-based simulation is much faster than the physical fatigue test, which usually costs 1 or 2 weeks to examine a single specimen. But it is still not efficient enough to apply in the PFCG model, as discussed before. Alternatively, the GPR model only spends about 0.05 ~ 0.08 s to perform a single solution. Thus, the prediction of a single specimen could be completed within 40 s, i.e., about 1875 times improvement in the computational efficiency compared with the FE-based analysis.

### 4.3. Result of prior PFCG model

Since the test data are not included yet, the established PFCG model is defined as the prior model, i.e., the model with prior knowledge only

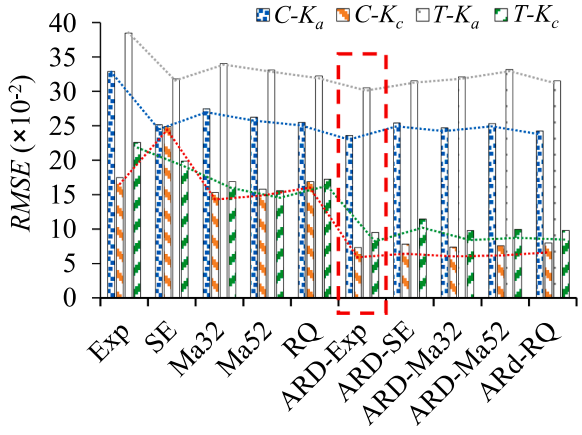


**Fig. 10.** Performance of various covariance function.

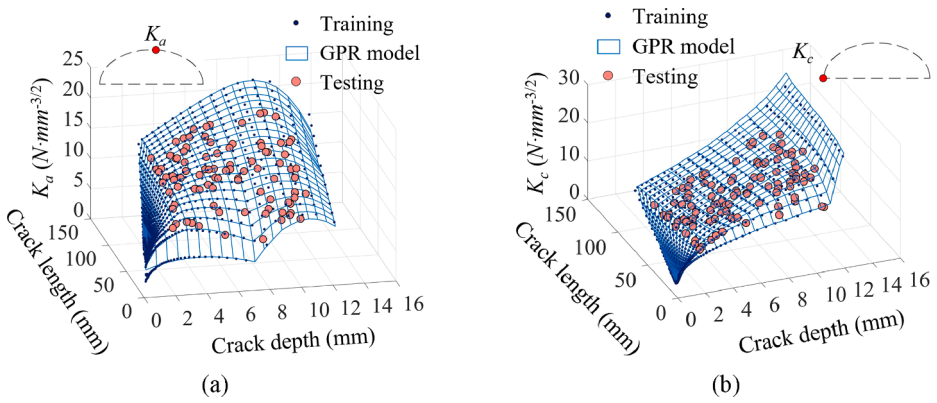


**Fig. 11.** Comparison of the SIF under 1kN force between the GPR prediction and FE results in Type C specimens, solved for: (a) Crack tip; (b) Crack edge.

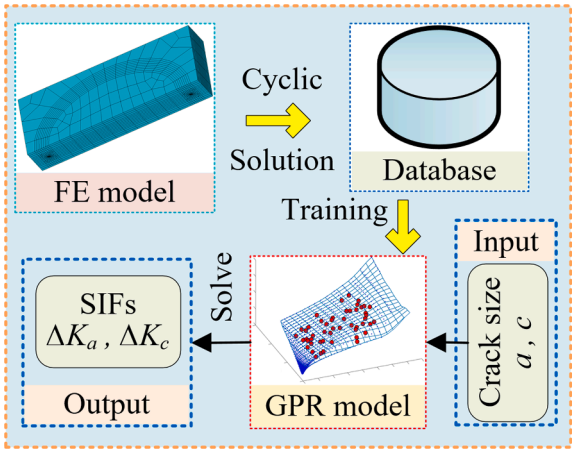


**Fig. 12.** Overview on the construction and application of the GPR model.

[56]. Based on the prior PFCG model, S-N data are generated under ten stress ranges, and 200 samples are simulated in each range. Fig. 13 shows the typical crack growth pattern predicted by the prior model. The result shows two cracking types, i.e., dual cracking and solo cracking. In the dual cracking pattern, two cracks co-exist while the larger crack causes failure. The solo cracking pattern also shows two cracks, including a large crack and a tiny one. However, the tiny crack is too small to identify by traditional means and has little influence on the fatigue performance of the RD joint. Thus, the pattern with a tiny secondary crack is simplified as the solo cracking pattern. In the qualitative view, the result by the PFCG model is highly consistent with the cracking pattern observed and measured from the experiments, as shown in Fig. 5, indicating the effectiveness of the PFCG model in predicting the cracking pattern of the tested specimens.

Based on the statistical approach suggested in [9], the result by the prior PFCG model is used to derive numerical P-S-N curves, including the mean curve and the design curve with a survival rate of 97.7%. The power index of $m = 3$ is also employed for the consistency with the experimental P-S-N curve. Figs. 14 and 15 show derived P-S-N curves in nominal stress and hot spot stress, respectively.

Compared with the experimental S-N curve in which the type T specimen illustrates a notable enhancement, the numerical curve by the prior PFCG model only results in a slight difference between the type C and type T specimen. Further comparison is made between the type C and type T specimens using the fatigue strength at 200 million cycles [56]. In terms of the nominal stress, both the mean and design curves of the type T specimen are about 4% higher than that of the type C specimen. Similarly, in terms of the hot-spot stress, the type-T specimen also illustrates a fatigue strength around 4% higher than that of the type-C specimen. A comparison is also made between the numerical result and the test data, as shown in Fig. 4. The numerical mean strength of type C specimens is 8% higher in nominal stress and 2% higher in hot-spot stress than that of test data. By contrast, the numerical value of type-T specimens is reduced by 9% in nominal stress and 12% in hot-spot stress, compared with the test data. Thus, calibration is required on the prior PFCG model to bridge the gap between fatigue test and numerical simulation, which is the key topic in the following sections.

## 5. Dynamic Bayesian network (DBN)-enhanced FCG analysis

### 5.1. Adaptation of DBN structure to fatigue deterioration

The Dynamic Bayesian network (DBN) [58] is a powerful tool for uncertainty propagation and quantification in probabilistic models.

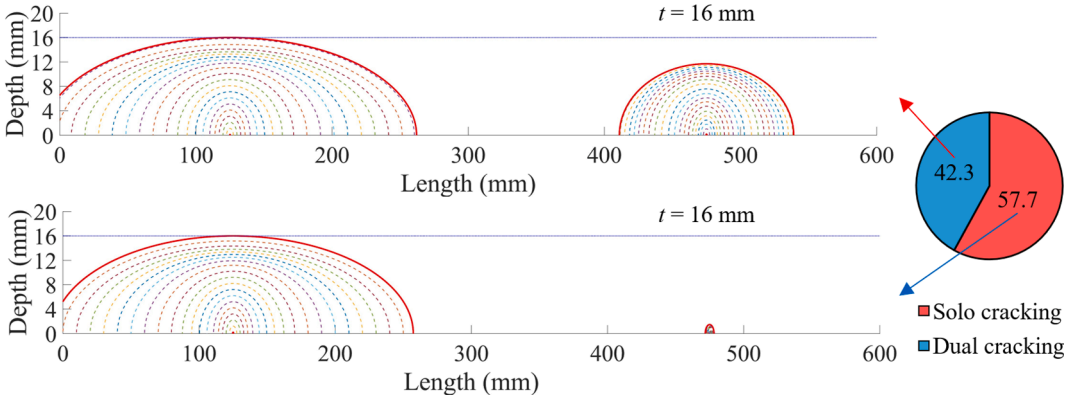


**Fig. 13.** Typical cracking patterns predicted by PFCG model.

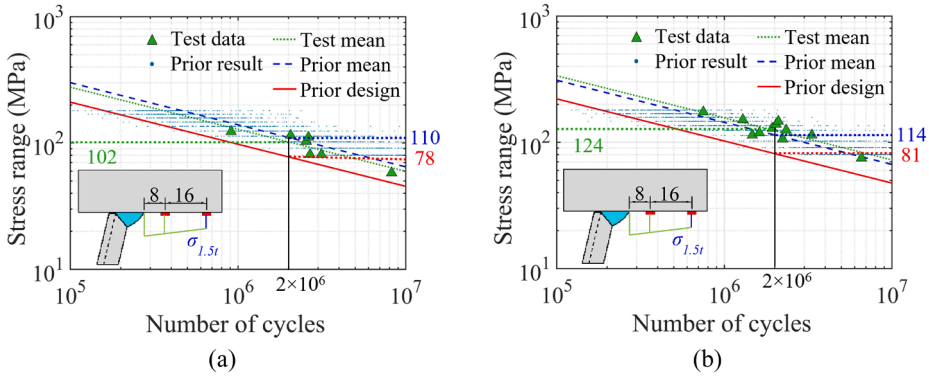


**Fig. 14.** Nominal S-N derived by the prior PFCG: (a) Type-C; (b) Type-T.

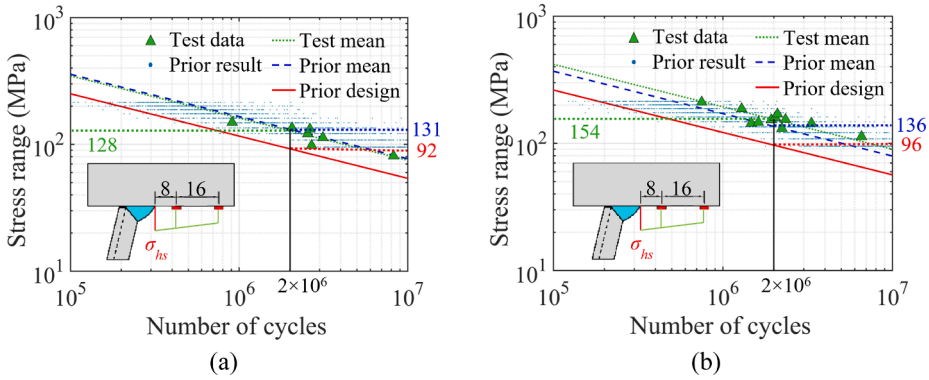


**Fig. 15.** Hot-spot S-N derived by the prior PFCG: (a) Type-C; (b) Type-T.

Fig. 16a depicts the general structure of the DBN. The DBN is naturally suitable for structural deterioration issues, and a list of fundamental works has already been made [59] (also confirmed by the literature [27 28 29] discussed before). With the DBN, uncertainties can be propagated between variables to conduct the forward prediction from state-to-response and the backward updating from evidence-to-state. Since the specimens have been fabricated by the same manufacturer under the same welding procedure, the correlation in the fatigue limit $\Delta K_{th}$ should be accounted for according to Maljaars and Vrouwenvelder [60]. The coefficient of correlation is determined as $\rho_{\Delta K_{th}} = 0.75$, based on the estimation of the entire distribution in [48] and the statistics from limited specimens in [61]. In simulating the correlation, a hierarchical model [62] is introduced to augment the DBN, as shown in Fig. 16b.

In the hierarchical model, a common uncertainty parameter $\alpha_V$ is proposed. The marginal distribution of correlated variables is assumed to be conditional on $\alpha_V$. The parameter $\alpha_V$ is assumed to follow the standard Gaussian distribution, and the cumulative distribution function (CDF) of variables can be expressed in the marginal form $F_{V|\alpha}(x)$, as shown in Equation (6):

$$F_{V|\alpha}(x) = \Phi\left(\frac{\Phi^{-1}(F_V(x)) - \sqrt{\rho_G} \bullet \alpha}{\sqrt{1-\rho_G}}\right) \tag{6}$$

where $F_V(x)$ is the uncorrelated CDF of variable $v$; $\Phi$ and $\Phi^{-1}$ are the CDF and inverse CDF of standard Gaussian distribution, respectively; $\rho_G$ is the equivalent correlation coefficient in standard Gaussian space, which is determined according to [64].

### 5.2. Development of DBN for PFCG model

The DBN is constructed for the PFCG model with the common uncertainty parameter, as shown in Fig. 17. The developed DBN consists of 4 types of nodes, including the variable node, deterministic node, functional node, and evidenced node.

The employed nodes are summarised in Table 4, including the variable, deterministic, functional and evidenced nodes. The initial value of variable nodes is determined as discussed before in Section 3.2 on the PFCG model and Section 5.1 on the common uncertainty parameter. During the DBN simulation, the functional nodes are solved step-by-step.

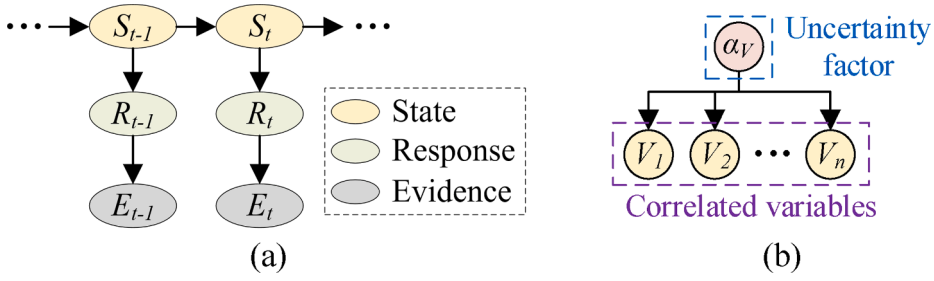


**Fig. 16.** DBN for fatigue deterioration: (a) general structure; (b) hierarchical model.

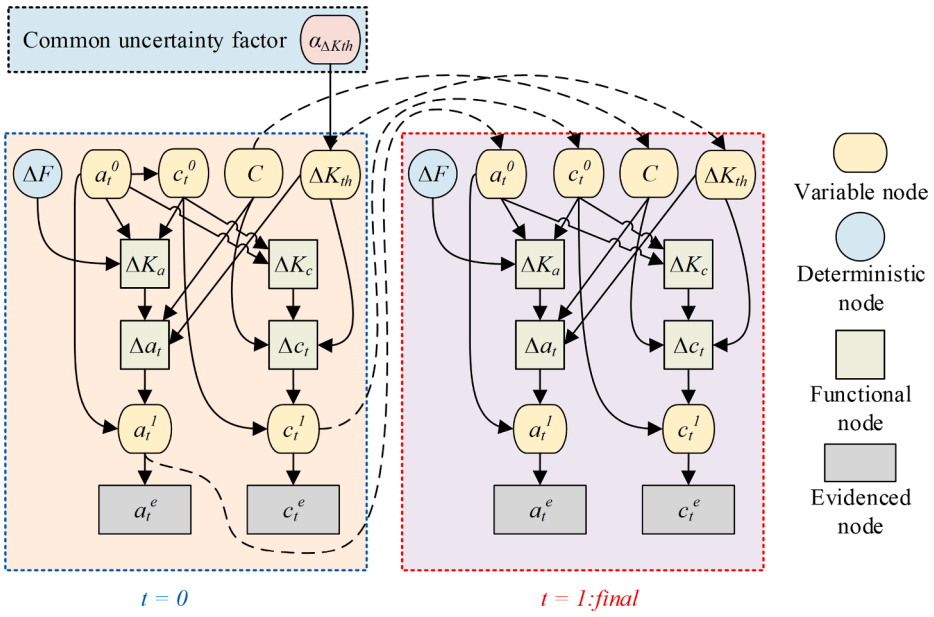


**Fig. 17.** DAG of the DBN for the PFCG model.

The evidenced nodes are determined after the measurement in Section 2.3. It is worth notating that the DBN at the first time slice ($t = 0$) is different from the one at rest time slices since the initial flaw length is conditional on the initial flaw depth.

### 5.3. Adaption of the solution algorithm

The inference algorithm is the core for uncertainty propagation in DBNs. The algorithm can be classified into the exact inference and approximate inference [65]. For DBNs constructed with continuous variables, the exact inference is usually not available [58], which may cause non-convergence problems in dealing with deterioration issues [66]. Thus, the variable in the DBN is discretised with non-uniform intervals. Fig. 18 shows the probability mass function of the initial crack depth transformed from the original probability distribution function.

The intervals are divided into the lower part, core part and upper part to approximate the different regions with different resolutions, by which a trade-off can be achieved between accuracy and efficiency. The core part is centred on the mean $\mu$ in Gaussian space, and its radius is set as the product of the characteristic value $K_V$ and the stand deviation $\sigma$ in Gaussian space. The percentage $P_V$ of intervals is allocated to the core part for intensification. The remaining intervals are assigned to the lower and upper parts according to their length. Table 5 summarises the variables and discretisation details.

**Table 4**
Nodes in the DBN.

| Node | Type | Description | Distribution |
|---|---|---|---|
| $\alpha_{\Delta K_{th}}$ | Variable | Common uncertainly factor of fatigue limit | $N(0,1)$ |
| $\Delta F$ | Deterministic | Range of applied cyclic force | By choices |
| $a_t^0$ | Variable | Initial crack depth at time $t$ | $a_0^0$ $LogN(0.15, 0.1)$ |
| $c_t^0$ | Variable | Initial crack half-length at time $t$ | $a_0^0/c_0^0$ $LogN(0.62, 0.25)$ |
| $C$ | Variable | Crack growth rate | $LogN(3.3, 1.6) \bullet 10^{-13}$ |
| $\Delta K_{th}$ | Variable | Fatigue limit | $LogN(140, 56)$ |
| $\Delta K_a$, $\Delta K_c$ | Functional | Calculated SIFs at crack tip and edge | By calculations |
| $\Delta a_t, \Delta c_t$ | Functional | Crack size increment at time $t$ | By calculations |
| $a_t^1, c_t^1$ | Variable | Final crack depth and length at time $t$ | By calculations |
| $a_t^e, c_t^e$ | Evidenced | Observed crack depth and length at time $t$ | By measurements |

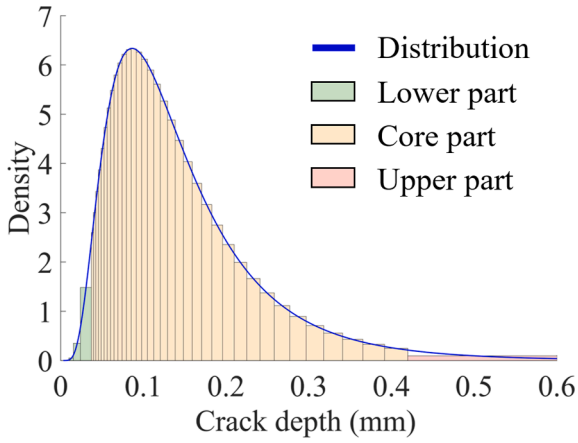


**Fig. 18.** Discretisation of initial crack depth.

A notable feature of the FCG process is the time-dependent variation in crack sizes. Thus, an adaptive interval is applied to the crack depth and half-length to improve accuracy. At the end of each time slice, the interval of crack sizes is re-discretised according to their new distribution. Fig. 19 shows the evolution in the interval of the crack depth in specimen C6 during the PFCG simulation (without updating). The core part moves right with cycles, suggesting the growth in crack depth.

The classic algorithm *frontier* [67] is applied to the constructed DBN to conduct exact inference. Since the DBN has a common uncertainty factor $\alpha_V$ to model the correlation, the original *frontier* algorithm is modified to enable the parallel updating of $\alpha_V$ by data from individual specimens, as illustrated by Equation 7:

$$L_i = P\left(E_{1:t}^i|\alpha_V\right) \propto \frac{P\left(\alpha_V|E_{1:t}^i\right)}{P(\alpha_V)} \tag{7a-7b}$$

$$P\left(\alpha_V|E_{1:t}^{1:N}\right) = P(\alpha_V) \bullet P\left(E_{1:t}^i|\alpha_V\right) \propto P(\alpha_V) \bullet \prod_{i=1}^{N} L_i$$

where $N$ denotes the number of specimens; $E_{1:t}^i$ and $E_{1:t}^{1:N}$ are the evidenced data from an individual specimen and all specimens, respectively; $L_i$ is the likelihood of specimens under the evidence $E_{1:t}^i$.

**Table 5**
Variable and discretization.

| Name | Symbol | Distribution | Range | $N_{Int}$ [1] | $D_V(v)$ [2] | $K_V$ [3] | $P_V$ [4] |
|---|---|---|---|---|---|---|---|
| Crack depth | $a$ | Lognormal | 0.01–40 ($mm$) | 50 | *Exp.* [5] | 2 | 0.75 |
| Crack length | $c$ | Lognormal | 0.01–300 ($mm$) | 50 | *Exp.* | 2 | 0.75 |
| Growth rate | $C$ | Lognormal | (4–200) × $10^{-14}$ | 20 | *Exp.* | 2 | 0.75 |
| Fatigue limit | $\Delta K_{th}$ | Lognormal | 20–420 ($N \bullet mm^{-3/2}$) | 20 | *Exp.* | 2 | 0.75 |
| Common uncertainty | $\alpha_{\Delta K_{th}}$ | Standard gaussian | −4–4 | 20 | *Uni.* [6] | 2 | 0.75 |

[1] Number of intervals;
[2] Discretisation function;
[3] Characteristic value;
[4] Percentage of core region;
[5] Exponential;
[6] Uniform.

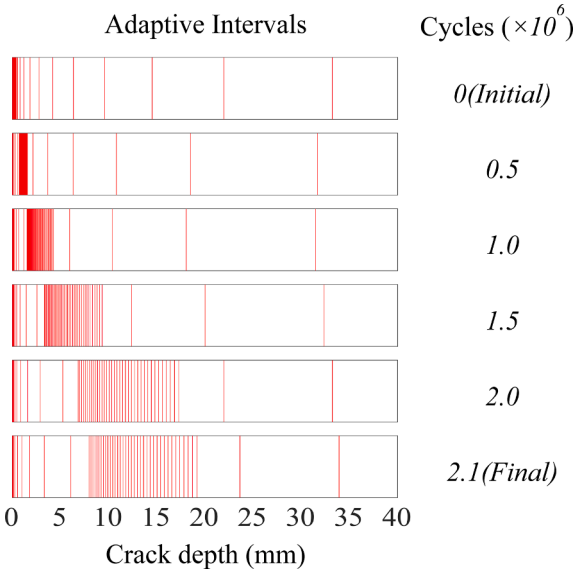


**Fig. 19.** Adaptive intervals of crack depth in specimen C6.

On this basis, the correlated variable (i.e., fatigue limit $\Delta K_{th}$ in this study) can be updated with the data from all the specimens by conditioned sampling using Equation (6).

### 5.4. Result and discussions

#### 5.4.1. DBN-based model updating

Based on the adapted DBN and inference algorithm, the prior PFCG model can be calibrated using the measured crack growth data. Fig. 20 shows the prediction of crack sizes in specimen T7, in which the calibration is made with the input of test data. Apart from the mean value, the upper and lower limits corresponding to the 97.7% survival rate are also included in Fig. 21 to reveal the evolution of uncertainties. Since no measurement is available for the crack size before the loading cycles of 1.5 million, the mean prediction follows the original PFCG model. Once the measured data are involved, a sudden change can be observed in the prediction curves, leading to convergence at the test measurement. After that, the prediction curves diverge with the number of cycles until they converge again at the next measurement. The prediction curve gradually matches with the test data, especially in means. As a result, the prior PFCG model is updated with measurement, which is defined as the posterior PFCG model.

Further comparison is carried out between the prior and posterior distribution of the fatigue limit. Fig. 21 shows the comparison in specimen T7. Compared with the prior distribution, the posterior

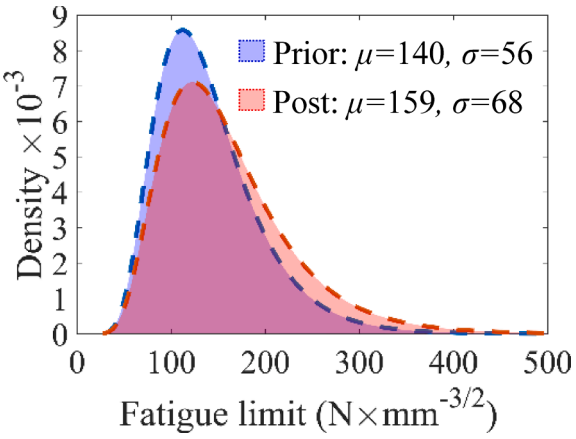


**Fig. 21.** Prior and posterior distribution of fatigue limit in specimen T7.

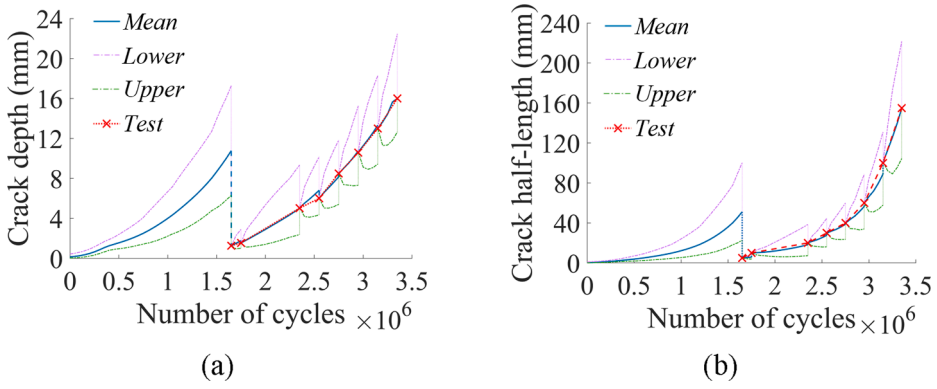


**Fig. 20.** Comparison of crack sizes between predicted mean and test of specimen T7: (a) Crack depth; (b) Crack half-length.

distribution shifts right, indicating an underestimated fatigue limit. The result can be related to the factor that the prediction of crack size is initially much higher than the measured size in specimen T7, as shown in Fig. 20. As the measurement is involved, the distribution of the fatigue limit is updated, and the posterior PFCG model gradually matches with the test data.

The prior and posterior distributions of the fatigue limit are illustrated in Fig. 22a and b for type-C and type-T specimens, respectively. In type-C specimens, the posterior distribution shifts left compared with the prior distribution (see Fig. 22a), indicating an overestimated fatigue limit. Accordingly, the fatigue life predicted by the original PFCG model is also overvalued, as evidenced in section 4.3. The posterior distribution becomes sharper than the prior distribution due to the reduced standard deviation, indicating the decrease in the uncertainty in the fatigue limit. As a result, the prediction accuracy also improves due to uncertainty propagation.

By contrast, the posterior distribution of type-T specimens shift right compared with the prior distribution (see Fig. 22b), suggesting an underestimated fatigue limit. Similarly, this could explain that the fatigue life prediction by the prior PFCG model is underrated. The uncertainty is also reduced as the standard deviation declines in the posterior distribution. As a result, the DBN updating can bridge the intrinsic gap between test data and the PFCG model.

#### *5.4.2. S-N result by the posterior PFCG model*

Based on the updated posterior PFCG model, P-S-N data are generated for type-C and type-T specimens. Figs. 23 and 24 show the generated P-S-N data and the mean and design curves derived using the same method as depicted in section 4.3. Compared with the result by the prior PFCG model (see Figs. 14 and 15), the P-S-N curve by the posterior model shifts down in type-C specimens and rises up in type-T specimens. Similar to the previous discussion, the comparison is also conducted between the test data and numerical simulation, using the mean fatigue strength at 2 million cycles. In type-C specimens, the difference is about 3% in both nominal and hot-sport stress. In type-T specimens, the difference becomes no more than 2%. In general, the maximum difference between the test and simulation is reduced from 12% to 3% since the prior PFCG model is updated into a posterior model. As a result, a notable improvement can be expected in the agreement between test data and predictions.

Meanwhile, fatigue design curves are established for RD joints, as shown in Figs. 23 and 24. For feasibility and conservativeness in engineering practices, the design curve of RD joints in type-C is recommended as FAT 75 in nominal stress and FAT 90 in hot-spot stress. This numerical result is highly similar to the design curve in the code AASHTO LRFD [68], in which FAT 70 and FAT 90 are respectively suggested in nominal stress and hot-spot stress. Similarly, the design curve of RD joints in type-T is suggested as FAT 90 in nominal stress and FAT 110 in hot-spot stress.

## 6. Conclusion and future suggestion

This study proposes a probabilistic fatigue crack growth (PFCG) model based on the fatigue test of rib-to-deck (RD) welded joints in orthotropic steel decks. The seven tested specimens are in two types, i.e., the type with conventional U-rib (type-C) and the type with thickened-edge U-rib (type-T). The proposed PFCG model is implemented using the Gaussian process regression (GPR) and updated by the dynamic Bayesian network (DBN) with the crack growth data measured from ten specimens (including four similar specimens tested in the previous study). The updated posterior PFCG model is employed to predict the fatigue life distribution of RD joints under various stress ranges, which supports the numerical derivation of probability-stress-life (P-S-N) curves. Based on the above works, the following conclusions can be drawn.

(1) The observed fatigue cracking pattern is similar to previous studies, i.e., the semi-elliptical crack initiates from the deck toe and then propagates in the thickness and length of the deck until failure. Compared with type-C specimens, the fatigue strength of RD joints in type-T specimens increases by 22% and 20% in nominal stress and hot-spot stress, respectively.
(2) A GPR model is trained by 2,000 FE samples to predict stress intensity factors for the PFCG simulation. The trained model is validated against 100 new FE samples, which shows satisfactory accuracy. Compared with the traditional step-by-step fatigue crack growth simulation, the FE-trained GPR model reduces the solution cost by approximately 1,875 times.
(3) A DBN is constructed to update the PFCG model with the fatigue crack growth data measured from ten specimens. Both the network structure and solution algorithm of the DBN is modified according to the PFCG model. By updating the prior PFCG model into a posterior model, the maximum discrepancy in the fatigue strength between prediction and test is reduced from 12% to 3%.
(4) Based on the updated posterior PFCG model, numerical P-S-N curves are derived for the classic type-C RD joint and the novel type-T RD joint. By adopting a survival rate of 97.7%, the fatigue design curves FAT 75 and FAT 90 are recommended for type-C RD joints in nominal stress and hot-spot stress, respectively. The type-T RD joint is suggested to check against the fatigue design curves FAT 90 and FAT 110 in nominal and hot-spot stress, respectively.

This study highlights the application of machine learning tools to assist the fatigue prediction of welded joints and update the fatigue model with measurements. The PFCG model in the present work is simplified to focus on a pioneered exploration and prototype verification. In further efforts, the more advanced XFEM can be used to include more physical details such as residual stress, multi-point crack initiation

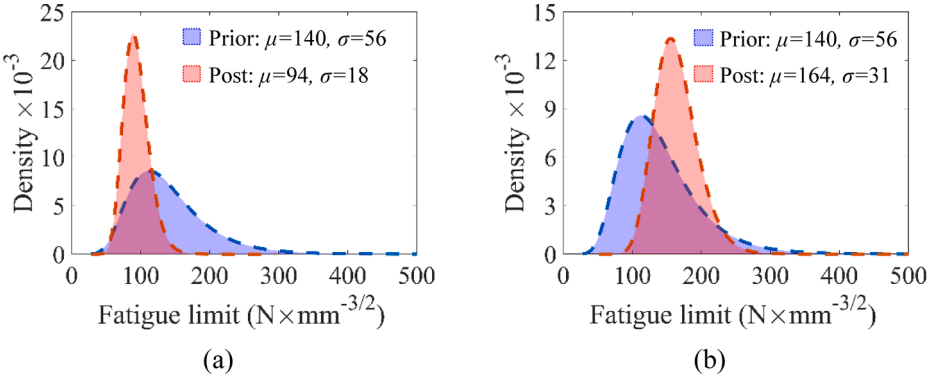


**Fig. 22.** Type-level prior and posterior distribution of fatigue limit: (a) type-C; (b) type-T.

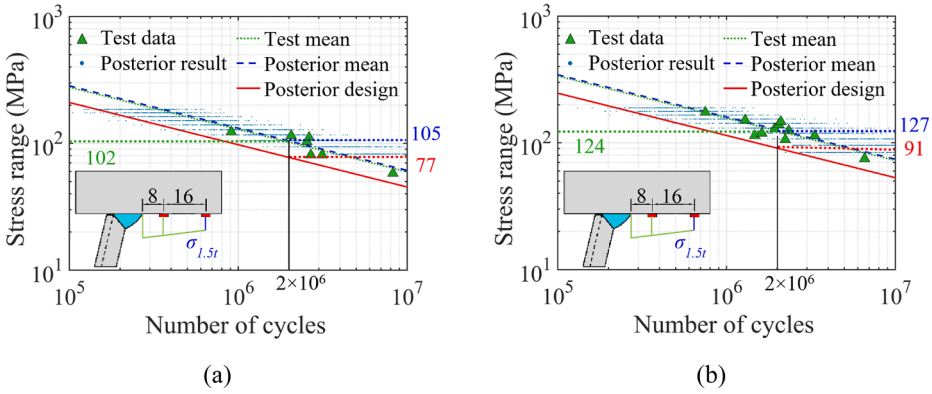


**Fig. 23.** Nominal stress-life curves by updated PFCG: (a) Type-C; (b) Type-T.

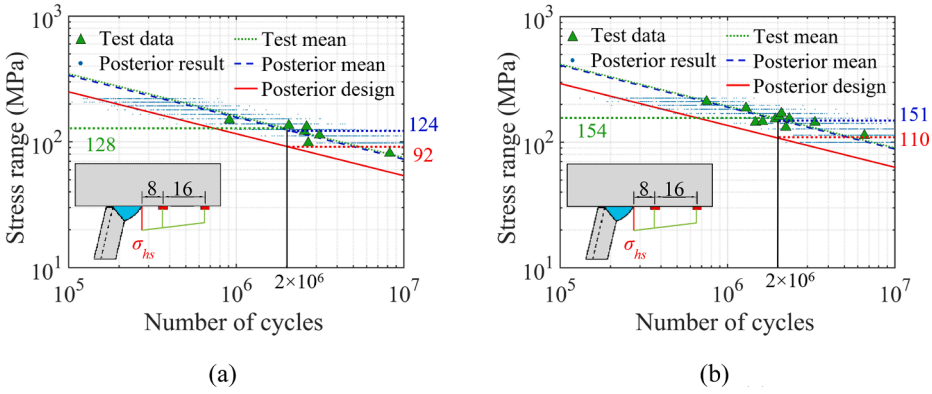


**Fig. 24.** Hot-spot stress-life curves by updated PFCG: (a) Type-C; (b) Type-T.

and coalescence, variation in crack front, crack closure, etc. Also, it is crucial to investigate the long-term fatigue deterioration of steel bridges (e.g., remain fatigue life estimation) based on the proposed P-S-N curves. Meanwhile, the training data in this study are from numerical predictions and laboratory tests, which leads to limitations in evaluating on-site steel bridges. Future works are recommended to incorporate the field data (e.g., by monitoring or inspection) along with the prediction and test. Besides, the GPR and DBN are combined in this study due to their proven feasibility. The application of more advanced algorithms can be explored in future works to enhance small sample-based training, such as the physic-guided neural network and Bayesian deep learning.

## CRediT authorship contribution statement

**Junlin Heng:** Methodology, Investigation, Formal analysis, Writing – original draft. **Kaifeng Zheng:** Conceptualization, Funding acquisition. **Xiaoyang Feng:** Validation, Data curation, Visualization, Project administration. **Milan Veljkovic:** Supervision, Writing – review & editing. **Zhixiang Zhou:** Supervision, Funding acquisition.

## Declaration of Competing Interest

The authors declare that they have no known competing financial interests or personal relationships that could have appeared to influence the work reported in this paper.

## *Acknowledgement*

The study is supported by the National Natural Science Foundation of China (grant number: 51778536) and Shenzhen Key Laboratory of Structure Safety and Health Monitoring of Marine Infrastructures (In preparation, grant number: ZDSYS20201020162400001).

## *Date Availability Statement*

Some or all the data, model or code data employed in this paper are available from the corresponding author upon reasonable request.

## References

[1] Chen S, Duffield C, Miramini S, Raja BNK, Zhang L. Life-cycle modelling of concrete cracking and reinforcement corrosion in concrete bridges: A case study. Eng. Struct. 2021;237:112143. https://doi.org/10.1016/j.engstruct.2021.112143.
[2] Connor R, Fisher J, Gatti W, Gopalaratnam V, Kozy B, Leshko B, et al. Manual for design, construction, and maintenance of orthotropic steel deck bridges. Washington, D.C., USA: Federal Highway Administration; 2012.
[3] Dooren F., Nagtegaal G., Ashurst D., Gration D., Blanken S., ander & Kunst, Pajc. (2010). Orthotropic Deck Fatigue: Renovation of 8 Bridges in the Netherlands. Structural Faults and Repair-2010: 13th International Conference. https://doi.org/10.13140/RG.2.1.1571.1200.
[4] Heng J, Zheng K, Gou C, Zhang Y, Bao Y. Fatigue performance of rib-to-deck joints in orthotropic steel decks with thickened edge u-ribs. J. BRIDGE ENG. 2017;22(9):04017059. https://doi.org/10.1061/(asce)be.1943-5592.0001095.
[5] Fisher JW, Roy S. Fatigue of steel bridge infrastructure. Struct. Infrastruct E. 2011;7(7):457–75. https://doi.org/10.1080/15732479.2010.493304.
[6] Shen, C. (1994). The statistical analysis of fatigue data, PhD Thesis, University of Arizona, Tucson, AZ, USA.
[7] Pipinato A, Pellegrino C, Bursi OS, Modena C. High-cycle fatigue behavior of riveted connections for railway metal bridges. J. Constr. Steel Res. 2009;65(12):2167–75. https://doi.org/10.1016/j.jcsr.2009.06.019.
[8] Pipinato A. Step level procedure for remaining fatigue life evaluation of one railway bridge. Balt. J. Road Bridge E. 2010;5(1):28–37. https://doi.org/10.3846/bjrbe.2010.04.
[9] Hobbacher A., Recommendations for fatigue design of welded joints and components, second ed., Springer, Switzerland, 2016. https://doi.org/10.1007/978-3-319-23757-2.
[10] Dong P. A structural stress definition and numerical implementation for fatigue analysis of welded joints. Int. J. Fatigue 2001;23(10):865–76. https://doi.org/10.1016/S0142-1123(01)00055-X.

[11] Niemi E, Fricke W, Maddox SJ. Fatigue analysis of welded components: designer's guide to the structural hot-spot stress approach, Woodhead publishing. Cambridge 2006. https://doi.org/10.1201/9781439824016.
[12] Madia M, Zerbst U, Beier HT, Schork B. The IBESS model–Elements, realisation and validation. ENG. Frac. Mech. 2018;198:171–208. https://doi.org/10.1016/j.engfracmech.2017.08.033.
[13] Xin H, Veljkovic M. Residual stress effects on fatigue crack growth rate of mild steel S355 exposed to air and seawater environments. Mater. Design 2020;2020:108732. https://doi.org/10.1016/j.matdes.2020.108732.
[14] Malschaert, D. (2020). Fracture Mechanics: Application on Orthotropic Steel Decks, Master Thesis, Delft University of Technology, Delft, The Netherlands. http://resolver.tudelft.nl/uuid:9cef6563-5e27-41a7-9b72-69c9036dd3d2.
[15] Liu, Y., Chen, F., Wang D., Lu, N. (2020). Fatigue crack growth behavior of rib-to-deck double-sided welded joints of orthotropic steel decks. Adv. Struct. Eng., 24(4), 136943322096175. https://doi.org/10.1177/1369433220961757.
[16] Wang B, Backer DH, Zhou XY, Chen A. Two-stage crack growth-based fatigue damage evaluation of orthotropic steel decks considering vehicle overload. Struct. Infrastruct. E. 2020;2020:1–14. https://doi.org/10.1080/15732479.2020.1759657.
[17] Berg N, Xin H, Veljkovic M. Effects of residual stresses on fatigue crack propagation of an orthotropic steel bridge deck. Mater. Design 2020;198(2021):109294. https://doi.org/10.1016/j.matdes.2020.109294.
[18] Gupta, R. (2019). Prediction of Fatigue Crack Propagation in Orthotropic Steel Decks using XFEM based on LEFM and VCCT, Master Thesis, Delft University of Technology, Delft, The Netherlands. https://repository.tudelft.nl/islandora/object/uuid%3Aef98f2f7-aa79-4bd1-b444-be8c2915eafe.
[19] Nagy W, Schotte K, Van Bogaert P, De Backer H. Fatigue strength application of fracture mechanics to orthotropic steel decks. Adv Struct Eng 2016;19(11):1696–709.
[20] Gupta RS, Xin H, Veljkovic M. Fatigue crack propagation simulation of orthotropic bridge deck based on extended finite element method. Procedia Struct Integrity 2019;22:283–90. https://doi.org/10.1016/j.prostr.2020.01.036.
[21] Kwon K, Frangopol DM, Soliman M. Probabilistic Fatigue Life Estimation of Steel Bridges by Using a Bilinear S-N Approach. J. Bridge Eng. 2012;17(1):58–70. https://doi.org/10.1061/(asce)be.1943-5592.0000225.
[22] Righiniotis TD, Chryssanthopoulos MK. Probabilistic fatigue analysis under constant amplitude loading. J. Constr. Steel. Res. 2003;59(7):867–86.
[23] Liu Y, Mahadevan S. Probabilistic fatigue life prediction using an equivalent initial flaw size distribution. Int. J. Fatigue 2009;31(3):476–87. https://doi.org/10.1016/j.ijfatigue.2008.06.005.
[24] Heng J, Zheng K, Kaewunruen S, Zhu J, Baniotopoulos C. Probabilistic fatigue assessment of rib-to-deck joints using thickened edge U-ribs. Steel Compos. Struct. 2020;2:23–56.
[25] Bowness D, Lee MMK. Prediction of weld toe magnification factors for semi-elliptical cracks in T–butt joints. Int. J. Fatigue 2000;22(5):369–87. https://doi.org/10.1016/S0142-1123(00)00012-8.
[26] Guzzi R. Data Assimilation: Mathematical Concepts and Instructive Examples, Springer. Switzerland 2016. https://doi.org/10.1007/978-3-319-22410-7.
[27] Straub D. stochastic modeling of deterioration processes through dynamic Bayesian networks. J. Eng. Mech. 2009;135(10):1089–99. https://doi.org/10.1061/(asce)em.1943-7889.0000024.
[28] Zhu J, Zhang W, Li X. Fatigue damage assessment of orthotropic steel deck using dynamic Bayesian networks. Int. J. Fatigue 2019;118:44–53. https://doi.org/10.1016/j.ijfatigue.2018.08.037.
[29] Heng J, Zheng K, Kaewunruen S, Zhu J, Baniotopoulos C. Dynamic Bayesian network-based system-level evaluation on fatigue reliability of orthotropic steel decks. Eng. Fail. Anal. 2019;105:1212–28. https://doi.org/10.1016/j.engfailanal.2019.06.092.
[30] Hu D, Su X, Liu X, Mao J, Shan X, Wang R. Bayesian-based probabilistic fatigue crack growth evaluation combined with machine-learning-assisted GPR. Eng. Fract. Mech. 2020;229:106933. https://doi.org/10.1016/j.engfracmech.2020.106933.
[31] Silva GC, Beber VC, Pitz DB. Machine learning and finite element analysis: An integrated approach for fatigue lifetime prediction of adhesively bonded joints. Fatigue Fract. Eng. M. 2021;44(12):3334–48. https://doi.org/10.1111/ffe.13559.
[32] Zhang Z, Sun C. Structural damage identification via physics-guided machine learning: a methodology integrating pattern recognition with finite element model updating. Struct. Health. Monit. 2021;20(4):1675–88. https://doi.org/10.1177/1475921720927488.
[33] Wang H, Yeung DY. Towards Bayesian deep learning: A framework and some existing methods. IEEE Trans Knowl Data Eng 2016;28(12):3395–408. https://doi.org/10.1109/TKDE.2016.2606428.
[34] Standardization Administration of China (SAC), GB/T 714-2015 Structural steel for bridge, Standards Press of China, Beijing, China, 2015.
[35] European committee for standardization (CEN), EN 10025:2019 Hot rolled products of structural steels, CEN, Brussels, Belgium, 2019.
[36] Standardization Administration of China (SAC), GB/T 8110-2020 Wire electrodes and weld deposits for gas shielded metal arc welding of non-alloy and fine grain steels, Standards Press of China, Beijing, China, 2020.
[37] Wang Q, Ji B, Li C, Fu Z. Fatigue evaluation of rib-deck welds: Crack-propagation-life predictive model and parametric analysis. J. Constr. Steel Res. 2020;173:106248. https://doi.org/10.1016/j.jcsr.2020.106248.
[38] MTS Systems Corporation. MTS hydraulic dynamic testing system. Eden Prairie, MA, US. https://www.mts.com/home.
[39] Guennec B, Ueno A, Sakai T, Takanashi M, Itabashi Y. Effect of the loading frequency on fatigue properties of JIS S15C low carbon steel and some discussions based on micro-plasticity behavior. Int. J. Fatigue 2014;66:29–38. https://doi.org/10.1016/j.ijfatigue.2014.03.005.
[40] Huneau B, Mendez J. Evaluation of environmental effects on fatigue crack growth behaviour of a high strength steel in a saline solution with cathodic protection. Int. J. Fatigue 2006;28(2):124–31. https://doi.org/10.1016/j.ijfatigue.2005.04.011.
[41] Feng X, Zheng K, Heng J, Lei M, Zhang Y. Studies on Fatigue Crack Propagation Pattern and Design S-N Curves of Rib-to-Deck Welded Joints in Orthotropic Steel Decks Using Thickened Edge U-Ribs. J. China Railway Society 2021;43(4):191–9.
[42] Dung CV, Sasaki E, Tajima K, Suzuki T. Investigations on the effect of weld penetration on fatigue strength of rib-to-deck welded joints in orthotropic steel decks. Int. J. Steel Struct. 2015;15(2):299–310.
[43] Li J. Research on formation mechanism and performance evaluation of dominant fatigue failure modes of orthotropic steel deck. Chengdu, China: Sothwest Jiaotong University; 2022. PhD Thesis.
[44] Luo P, Zhang Q, Bao Y, Bu Y. Fatigue performance of welded joint between thickened-edge U-rib and deck in orthotropic steel deck. Eng. Struct. 2019;181:699–710. https://doi.org/10.1016/j.engstruct.2018.10.030.
[45] Baik B, Yamada K, Ishikawa T. Fatigue crack propagation analysis for welded joint subjected to bending. Int. J. Fatigue 2011;33(5):746–58. https://doi.org/10.1016/j.ijfatigue.2010.12.002.
[46] British Standards Institution (BSI). BS 7910:2015 Guide to methods for assessing the acceptability of flaws in metallic structures, BSI Standards Limited, London, UK, 2015.
[47] Kountouris IS, Baker MJ. Defect assessment: analysis of the dimensions of defects detected by ultrasonic inspection in an offshore structure, CESLIC Report OR8. London, UK: Imperial College of Science and Technology; 1989.
[48] Austen, I. (1983). Measurement of fatigue crack threshold value for use in design. BSC Report SH/EN/9708/2/83/B, British Steel Corporation, London, UK.
[49] ANSYS. Engineering Simulation and 3D Design Software; ANSYS Inc., Canonsburg, USA. http://www.ansys.com/.
[50] ANSYS (2020). Mechanical APDL Documentation, ANSYS Inc., Canonsburg, PA, USA.
[51] Taylor D, Hoey D. High cycle fatigue of welded joints: The TCD experience. Int. J. Fatigue 2009;31(1):20–7. https://doi.org/10.1016/j.ijfatigue.2008.01.011.
[52] Anderson TL. Fracture mechanics: fundamentals and applications. 4th edition. Boca Raton, FL, US: CRC Press; 2017.
[53] Rasmussen, C.E., & Nickisch, H. (2010). Gaussian processes for machine learning (GPML) toolbox. J MACH. LEARN. RES., 11, 3011-3015. https://dl.acm.org/doi/10.5555/1756006.1953029.
[54] Kim, N. H., An, D., & Choi, J. H. Prognostics and health management of engineering systems. Springer International Publishing, Switzerland, 2017. https://doi.org/10.1007/978-3-319-44742-1.
[55] Cressie N. The origins of kriging. Math. Geol. 1990;22(3):239–52. https://doi.org/10.1007/BF00889887.
[56] Korb KB, Nicholson AE. Bayesian artificial intelligence. Boca Raton, FL, US: CRC Press; 2010.
[58] Murphy, K. P., & B.A. (2002). Dynamic Bayesian Networks: Representation, Inference and Learning. PhD Thesis, University of California, Berkeley, USA, 2002. https://doi.org/10.1017/CBO9781107415324.004.
[59] Luque J, Straub D. Reliability analysis and updating of deteriorating systems with dynamic Bayesian networks. Struct. Saf. 2016;62:34–46. https://doi.org/10.1016/j.strusafe.2016.03.004.
[60] Maljaars J, Vrouwenvelder ACWM. Probabilistic fatigue life updating accounting for inspections of multiple critical locations. Int. J. Fatigue 2014;68(11):24–37. https://doi.org/10.1016/j.ijfatigue.2014.06.011.
[61] Ohta A, Suzuki N, Maeda Y. Unique fatigue threshold and growth properties of welded joints in a tensile residual stress field. Int J Fatigue 1997;19(93):303–10.
[62] Raudenbush SW, Bryk AS. Hierarchical linear models, applications and data analysis methods. 2nd edition. US: SAGE Publications CA; 2008.
[64] Noh Y, Choi KK, Du L. Reliability-based design optimization of problems with correlated input variables using a Gaussian Copula. Struct Multidiscip Optim 2009;38(1):1–16.
[65] Li C, Mahadevan S. Efficient approximate inference in Bayesian networks with continuous variables. RELIAB. ENG. SYST. SAFE. 2018;169:269–80. https://doi.org/10.1016/j.ress.2017.08.017.
[66] Schneider R, Thöns S, Straub D. Reliability analysis and updating of deteriorating systems with subset simulation. STRUCT. SAF. 2017;64:20–36. https://doi.org/10.1016/j.strusafe.2016.09.002.
[67] Murphy, K., & Weiss, Y. (2013). The factored frontier algorithm for approximate inference in DBNs. arXiv preprint arXiv:1301.2296.
[68] AASHTO, AASHTO LRFD bridge design specifications, 9th edition. Washington, D. C., US, 2020.

## Further reading

[57] European committee for standardization (CEN), EN 1993: Eurocode 3 – design of steel structures, CEN, Brussels, Belgium, 2005.
[63] Bucher C. Computational analysis of randomness in structural mechanics: Structures and infrastructures book series. Boca Raton, FL, US: CRC PRESS; 2009.